CORA Cork Open Research Archive
Cartlann Taighde Oscailte Chorcaí

Title	Persistence of ferroelectricity close to unit-cell thickness in structurally disordered Aurivillius phases
Authors	Keeney, Lynette;Saghi, Zineb;O'Sullivan, Marita;Alaria, Jonathan;Schmidt, Michael;Colfer, Louise
Publication date	2020-12-01
Original Citation	Keeney, L., Saghi, Z., O'Sullivan, M., Alaria, J., Schmidt, M. and Colfer, L. (2020) 'Persistence of ferroelectricity close to unit-cell thickness in structurally disordered Aurivillius phases', Chemistry of Materials, 32(24), pp. 10511-10523. doi: 10.1021/acs.chemmater.0c03454
Type of publication	Article (peer-reviewed)
Link to publisher's version	10.1021/acs.chemmater.0c03454
Rights	© 2020, American Chemical Society. This document is the Accepted Manuscript version of a Published Work that appeared in final form in Chemistry of Materials, after technical editing by the publisher. To access the final edited and published work see https://doi.org/10.1021/acs.chemmater.0c03454
Download date	2026-10-30 12:06:26
Item downloaded from	https://hdl.handle.net/10468/10951

UCC
University College Cork, Ireland
Coláiste na hOllscoile Corcaigh

Persistence of ferroelectricity close to unit-cell thickness in structurally disordered Aurivillius phases

Lynette Keeney[1]*, Zineb Saghi[2], Marita O'Sullivan[3], Jonathan Alaria[3], Michael Schmidt[1], Louise Colfer[1]

1. Tyndall National Institute, University College Cork, 'Lee Maltings', Dyke Parade, Cork, T12 R5CP, Ireland.
2. Université Grenoble Alpes, CEA, LETI, Grenoble, F-38000, France.
3. Department of Physics, University of Liverpool, Liverpool, L69 7ZE, UK.

ABSTRACT: Multiferroics intertwine ferroelectric and ferromagnetic properties, allowing for novel ways of manipulating data and storing information. To optimize the unique $Bi_6Ti_xFe_yMn_zO_{18}$ (B6TFMO) multiferroic, ultra-thin (<7 nm) epitaxial films were synthesized by direct liquid injection chemical vapor deposition (DLI-CVD). Epitaxial growth is however confounded by the volatility of bismuth, particularly when utilizing a post-growth anneal at 850 °C. This results in microstructural defects, intergrowths of differing Aurivillius phases and formation of impurities. Improved single-step DLI-CVD processes were subsequently developed at 710 °C and 700 °C, enabling lowering of crystallization temperature by 150 °C and significantly enhancing film quality and sample purity. Ferroelectricity is confirmed in 5 nm (1 unit-cell thick) B6TFMO films, with tensile epitaxial strain enhancing the piezoresponse. In-plane ferroelectric switching is demonstrated at 1.5 unit-cell thickness. The persistence of stable ferroelectricity near unit-cell thickness in B6TFMO, both in-plane and out-of-plane, is significant and initiates possibilities for miniaturizing novel multiferroic-based devices.

INTRODUCTION: Multiferroic materials, possessing simultaneous ferroelectric and ferromagnetic memory states, have been identified[1,2] as promising energy-efficient architectures for memory scaling beyond current technologies. The unique potential of single-phase multiferroics lies in the creation of a multi-state storage device based on simultaneous electroresistance and magnetoresistance states when electrons tunnel through an ultra-thin multiferroic tunnel junction.[3] No such working devices presently exist however as single-phase room temperature (RT) multiferroics are exceedingly scarce[4-6] and their material properties are currently limited. While $Pb(Zr,Ti)O_3$-$Pb(Fe,Ta)O_3$[5] and $(Ca_ySr_{1-y})_{1.15}Tb_{1.85}Fe_2O_7$[6] are promising RT single-phase multiferroics, they have so far only been synthesized in ceramic (bulk) form. Bulk samples[6] of mutiferroic $(BiTi_{0.1}Fe_{0.8}Mg_{0.1}O_3)_{0.85}(CaTiO_3)_{0.15}$ have magnetic moments of 6.49 emu/cm^3, however only weak magnetic signals are reported for thin films.[7,8] $BiFeO_3$ (BFO) is the best-known RT single-phase multiferroic material, and epitaxial strain in thin films has enabled tuning of ferroelectric polarization and magnetic moment.[9] Indeed, 45 nm La-substituted BFO ($La_{0.1}Bi_{0.9}FeO_3$, LBFO) has been utilized[1,2] in a magnetoelectric spin-orbit coupled (MESO) logic device; although practical use of this device relies on considerable material development to enable coercive fields and switching voltages (18.6 kV/cm and 100 mV) much lower than required by LBFO (>200 kV/cm and 1 V). In addition, magnetic order in BFO is primarily antiferromagnetic and only displays a weak, canted ferromagnetic moment whose cycloidal magnetic order prohibits linear magnetoelectric coupling. This is incompatible with low-energy spintronics.

Aurivillius bismuth-based materials (general formula $(Bi_2O_2)(A_{m-1}B_mO_{3m+1})$) are naturally 2*D* (two dimensional) nanostructured, where $(Bi_2O_2)^{2+}$ fluorite-type layers are interleaved with *m* numbers of perovskite-type units (**Fig. S1**). They are established ferroelectrics, with high Curie temperatures (>600°C) and large in-plane spontaneous polarizations. $SrBi_2Ta_2O_9$ (m = 2) and $Bi_{3.25}La_{0.75}Ti_3O_{12}$ (m = 3) Aurivillius phases can be integrated onto CMOS compatible substrates[10] and have been developed for commercial use in Fe-RAM (ferroelectric random access memory) devices.[11-13] The Aurivillius phase $Bi_6Ti_xFe_yMn_zO_{18}$ (B6TFMO; x = 2.80 to 3.04; Y = 1.32 to 1.52; Z = 0.54 to 0.64) system is a rare example of a single-phase RT multiferroic to challenge BFO[14], displaying saturation magnetization (M_S) values of 215 emu/cm^3 and in-plane saturation polarization (P_s) values of >26 μC/cm^2.[15-19] B6TFMO possesses 5 perovskite blocks per half unit-cell (*m* = 5) (**Fig. S1**) and is the only multiferroic material demonstrating intrinsic ferroelectric/ferromagnetic properties to a defined confidence level (≥99.5%) in thin film form (~100 nm). Individual B6TFMO Aurivillius phase grains demonstrate the reversible magnetoelectric switching necessary for practical magnetoelectric device applications.[17,18] The preference for manganese cations to position to the center-most layer of the B6TFMO structure is important for multiferroic behavior.[16]

While earlier work focused on non-epitaxial, 100 nm-thick B6TFMO films, a crucial requirement for materials targeted for miniaturized data storage applications is the enhancement of their functional properties at sub-10 nm dimensions.[20] This is a challenge for multiferroic materials, since ferroelectricity

is a collective phenomenon and the spontaneous electrical polarization is expected only to be sustained above some critical thickness.[21]

Recently we have shown that out-of-plane ferroelectricity can persist and switch in exfoliated $Bi_5Ti_3Fe_{0.5}Co_{0.5}O_{15}$ Aurivillius phase nano-flakes with thicknesses of only 2.4 nm, which equates to one-half of the normal crystal unit-cell (0.5 u.c.).[22] The ultrasonic exfoliation method generates 2*D* nano-structures by cleaving the Aurivillius structure at the $(Bi_2O_2)^{2+}$ layers to yield flakes with linear dimensions many times the flake thickness. However the flake thickness or diameter cannot accurately be controlled using the liquid ultrasonic exfoliation technique. A range of flake sizes were observed (lateral diameters of 80 nm to 700 nm with thicknesses of 2.4 to 120 nm) as individual flakes, or stacked on top of each other, or overlapped together in clusters.[22] Accurate control of thickness and the production of larger lateral dimensions are prerequisites for the wider application of ultra-thin multiferroics.

In order to increase their technological potential for utilization in future devices, the focus of this contribution was the development of an industrially-scalable direct liquid injection chemical vapor deposition (DLI-CVD) process for the synthesis of 2*D* epitaxial B6TFMO films of sub-10 nm thickness. DLI-CVD is a versatile thin-film growth process meeting industry requirements of high through-put, excellent control of stoichiometry and thickness, large area uniformity for scale-up and allows for conformal coating of complex structures. Epitaxial growth is necessary in order to produce well-defined multiferroic films with controlled orientation. Furthermore, epitaxial strain enables tuning of ferroelectric polarization and is predicted to control the distribution of magnetic cations within the Aurivillius phases.[23] Substrates allowing epitaxial matches to the Aurivillius structure ($SrTiO_3$ (STO), $La_{0.26}Sr_{0.76}Al_{0.61}Ta_{0.37}O_3$ (LSAT) and $NdGaO_3$ (NGO)) enabled growth of continuous ultra-thin (< 7 nm) layers. Unfortunately, epitaxial growth of these complex oxides is confounded by the volatility of the bismuth species.[24] Whereas a two-step method utilizing a post-anneal at 850 °C resulted in samples complicated with several impurity phases, an enhanced single-step process was subsequently developed in this study which enabled the growth temperature to be lowered by 150 °C and considerably improved thin film quality and sample purity. The presence of trace levels (even below 0.1 vol. %) of magnetic impurities would complicate attempts to measure a magnetic signal intrinsic to the main B6TFMO Aurivillius phase,[15,17-19,25,26] therefore work was directed towards exploring the ferroelectric properties of these ultra-thin samples.

We present the first demonstration of ferroelectricity in sub-10 nm 2*D* films of the multiferroic B6TFMO system. Piezoresponse force microcopy (PFM) evidence for ferroelectricity in 5 nm films, equating to 1 u.c. of the normal crystal structure, is confirmed at RT and at 120 °C, with tensile epitaxial strain enhancing the piezoresponse. In-plane ferroelectric switching at RT in 1.5 u.c. thick (7 nm) B6TFMO demonstrates its potential for use in technologically competitive data storage devices based on in-plane tunnel junctions. Given that ferroelectric polarization is parallel to the surface for all lateral directions,[27] devices based on in-plane memory architectures would not be hindered by competing depolarization fields[28] upon scaling down to ultra-thin dimensions.[29] For tunnel junction devices, this means that higher ON:OFF tunneling current ratios may be achieved with non-destructive read operations.[29-32] This work describes the progress in the optimization of multiferroic B6TFMO towards accomplishing the goal of eight-state information storage.[33]

EXPERIMENTAL SECTION:

THIN FILM DEPOSITION: B6TFMO thin films were prepared with a horizontal flow AIXTRON AIX 200/4FE AVD (atomic vapor deposition, or direct liquid injection chemical vapor deposition (DLI-CVD))[34,35] system. Bismuth, iron and titanium precursor solutions were commercially available from Epivalence Ltd. These were 0.1 mol dm^{-3} solutions of $Bi(thd)_3$, $Fe(thd)_3$ and $Ti(O\text{-}iPr)_2(thd)_2$ (where thd = 2,2,6,6-tetramethyl 3,5-heptanedionate; O-iPr = isopropoxide) in toluene and were maintained under N_2(g) (nitrogen gas) in stainless steel bubbler vessels. $Mn(thd)_3$ (99%, STREM chemicals) was dissolved in anhydrous toluene (99.8%, Sigma-Aldrich) under N_2(g) into a stainless steel bubbler vessel to a concentration of 0.025 mol dm^{-3} and used as manganese precursor. The pressure of the growth chamber was kept at 9 mbar. The growth chamber was a typical cold wall reactor with a susceptor heated substrate holder maintained at either 630 °C, 700 °C or 710 °C by means of an infra-red lamp assembly. In this study, the two step-process developed in Faraz *et al.*[17] using a DLI-CVD growth temperature of 630 °C and a post-anneal at 850 °C, was compared to a newly developed single-step process with a DLI-CVD growth temperature of either 700 °C or 710 °C without any post-anneal step. The liquid precursors were injected individually with the aid of inert N_2(g) carrier gas into a vaporizer maintained at 220 °C, using four individual injectors, one for each precursor source. The injected precursor volume (in the micro-liter range) was controlled by adjusting the numbers of discrete pulses (between 75 and 1000 injections for each precursor, depending on desired film thickness (between 5 nm to 100 nm)) and the opening time of injector (between 1.3 to 11.3 ms) for each pulse during a continuous injection mode at a frequency of 1 Hz. The amount of precursor injected was monitored with a liquid flow meter. The net volumetric precursor injection ratios were approximately 2.9:1.5:0.6 for $Ti(O\text{-}iPr)_2(thd)_2$, $Mn(thd)_3$ and $Fe(thd)_3$, respectively. Due to its relatively high volatility, 25% excess of the bismuth precursor was employed for samples requiring post-anneal at 850 °C (two-step process) as documented in the literature[17,36] and between 5-8% excess of $Bi(thd)_3$ was utilized for samples synthesized at 700 °C and 710 °C by the single-step process. The evaporated precursors were then transported through lines maintained at 220 °C into a showerhead and mixed with reactive gas (O_2(g) (oxygen gas)) to allow deposition on to the heated substrates. The total N_2(g) / O_2(g) flow in the growth chamber was 3000 sccm, of which O_2(g) flow was 1000 sccm. The substrates used in this study were single side polished c-m plane (0001) sapphire and (100) oriented STO, LSAT and NGO with average dimensions 10 x 10 x 0.5 mm. The substrates were cleaned with isopropyl alcohol followed by distilled water and dried using N_2(g). They were then rotated with 60 sccm N_2(g) flow through a susceptor holder to permit improved uniformity.

PHYSICAL CHARACTERIZATION: The crystalline properties of the films were characterized in **Fig. 2**, **3** and **Fig. S6 (a)** using a Panalytical MRD X-ray diffraction (XRD) system with filtered Cu Kα radiation source (45 kV and 40 mA) over the range $5° \leq 2\theta \leq 50°$. Further X-ray diffraction was carried out in **Fig. 4** using a Rigaku Smartlab with a 9 kW Cu rotating anode, a 2-bounce Ge monochromator and a Hypix detector. Out-of-plane scans in a standard symmetric θ/2θ configuration and rocking curves, where the sample was tilted by varying ω at a fixed 2θ angle, were performed to assess the phase purity and crystalline quality of the samples. Reciprocal space maps (RSMs) were collected using asymmetric ω-2θ scans to confirm the epitaxial relationship between the substrate and the films and to investigate the presence of strain. For the transmission electron microscopy (TEM) characterization, the samples were gold-coated to prevent charging, followed by platinum and carbon coatings to enable FIB cross sectioning. Cross-sections were prepared using a FEI Helios Nanolab 600i DualBeam focused ion beam-scanning electron microscope (FIB-SEM) (final thinning conditions: 93 pA current at 30 kV, final polish conditions: 47 pA current at 5 kV). Micro-structural analysis by high resolution TEM (HR-TEM) was conducted on a JEOL 2100 TEM, at 200 kV. High resolution scanning TEM (HR-STEM) imaging and energy dispersive X-ray (EDX) analysis were performed on a FEI Titan Themis operating at 200 kV and equipped with a probe spherical aberration corrector and a Super-X EDX system (four windowless silicon drift detectors). Surface chemical analysis was also performed using the FEI Helios NanoLab 600i operating at 20 kV and equipped with an Oxford X-Max 80 detector. Commercial atomic force microscopes (AFM), MFP-3D™, Asylum Research in AC mode (with Olympus AC240TS probes, Al reflex coated, 15 nm tip radius, 70 kHz resonant frequency) and Bruker Dimension Icon in PeakForce Tapping mode (with Bruker SCANASYST-AIR probes, Al reflex coated, 2 nm tip radius, 70 kHz resonant frequency) were used for topography mapping of the films.

NANO-SCALE FERROELECTRIC MEASUREMENTS: Electromechanical responses of the films were measured by PFM using an Asylum Research MFP-3D™ AFM in contact mode equipped with a HVA220 Amplifier for PFM and a cantilever scan angle of 90°. The Single Frequency mode (drive frequency = 15 kHz) enabled measurements of lateral and vertical piezoresponses where the Inverse Optical Lever Sensitivity of the cantilevers was calibrated according to the MFP-3D Procedural Operation 'Manualette', the system inherent background was determined using a non-piezoelectric silicon wafer and the PFM signal was then calibrated using α-quartz as a reference sample. The Dual AC (alternating current) Resonance Tracking Piezoresponse Force Microscopy (DART-PFM)[37] mode was used to boost both the vertical and lateral piezo signals. In this mode, the PFM signal is measured at the tip-sample contact resonance frequency, with higher signal-to-noise ratio compared with other frequencies. Topographical cross-talk is reduced using an amplitude feedback loop which tracks the contact resonance frequency so that drive frequencies are adjusted accordingly as the probe scans over the changing sample topography. Application of an AC bias to a conductive tip during contact mode imaging ($V_{tip} = V_{AC}\cos(\omega t)$) results in surface displacement (*d*) and deflection of cantilever due to the converse piezoelectric effect, with both normal and in-plane components. Piezoresponse is defined in the vertical/normal direction, ΔZ, as $\pm d_{zz}V_{AC}\cos(\omega t + \theta)$ and in the lateral/in-plane directions, $\Delta L_1 = \pm d_{zx}V_{AC}\cos(\omega t + \theta)$ and $\Delta L_2 = \pm d_{zy}V_{AC}\cos(\omega t + \theta)$, where ω = angular frequency; t = time; θ = phase (0° or 180°). The definition for piezoresponse can be manipulated to Acosθ, which allows us to visualize the magnitude of the piezoresponse through the PFM amplitude (A) images and the direction of the polarization via the PFM phase (θ) images.[38] Olympus AC240TM Electrilevers, Ti/Pt coated silicon probes (Al reflex coated, 15 nm tip radius, 70kHz resonant frequency) were used for PFM and topography imaging. Apex Super Sharp diamond probes AD-2.8-SS (Au reflex coated, <5 nm tip radius, 75 kHz resonant frequency, boron doped) were used to investigate possible in-plane anisotropy (**Fig. 7**, **Fig. S10** and **Fig. S11)**. The angular torsion of the cantilever as it oscillates was monitored in lateral PFM (LPFM) measurements, which were conducted in a similar manner to the vertical PFM (VPFM) measurements except the 'InFast' option was programmed to 'Lateral' as opposed to 'AC Deflection' and the drive frequencies were operated near contact resonance for lateral (670-720 kHz) and vertical (250-280 kHz) modes respectively with probing signals of between 1.0 to 3.0 V_{AC}, to enhance the signal-to-noise ratio. Imaging of the same sample area by VPFM and LPFM allows complementary mapping of the normal component of the piezoresponse vector (out-of-plane direction) and the transversal component of the in-plane piezoresponse (perpendicular to the cantilever axis), respectively.[39] There are no microscopic topographic markers on the surface and the same location cannot be found after physical sample rotation, thus preventing 3D-PFM imaging (VPFM and x, y-LPFM) and determination of the individual elements of the piezoelectric tensor.[39] Temperature controlled measurements were performed at 120 °C by securing samples on an Asylum Research PolyHeater modular heating stage. Ferroelectric lithography was performed using the Asylum Research PFM Lithography mode by converting an imported greyscale image into a bias map and employing direct current (DC) voltages of ±5.0V. The "write step" and VPFM imaging were performed with InFast set to 'AC Deflection' and LPFM imaging was performed with InFast set to 'Lateral'.

RESULTS AND DISCUSSION:

2. DLI-CVD Investigations:

2.1. Two-step process:

In previous work[17], approximately 100 nm thick B6TFMO films were prepared on c-m plane sapphire substrates by a two-step DLI-CVD process. Sapphire substrates were chosen for their cost-effectiveness and because they are chemically stable at the processing temperatures used to crystallize the Aurivillius phases. Although Si(100) and α-quartz are also cost-effective, previous studies[25] demonstrate that a reaction between the bismuth-containing Aurivillius phases and silicon tends to occur to at the interface between film and substrate to form an amorphous Bi_2O_3-SiO_2 phase (e.g. $Bi_4Si_3O_{12}$) on cooling. The aforementioned[17] process involved DLI-CVD deposition at 630 ˚C to form films that were amorphous in nature, followed by a post-anneal step at 850 ˚C which enabled crystallization of m = 5 B6TFMO. In this

contribution, attempts to synthesize sub-10 nm B6TFMO films using this two-step process were trialed by reducing the number of precursor injections from 1000 in previous work, to 100 injections per precursor in this work. Use of sapphire substrates, which in the past have been successfully deployed for the growth of thicker films, failed in attempts to use them as templates for ultra-thin Aurivillius phase growth. As shown in **Fig. S2 (a)-(b)**, continuous ultra-thin Aurivillius layers on sapphire substrates could not be achieved when such lower precursor saturation concentrations were utilized. Using the equation (a_p' = $1.33r_B$ + $0.6r_A$ + 2.36 Å) described by Newnham and Armstrong[40] and by employing an eight-fold coordinated radius value[41] for A-site Bi^{3+} (r_A) and average six-fold coordinated radii values[42] for the B-site ions (r_B), a value of 3.89 Å was calculated for the theoretical pseudo-lattice parameter of the perovskite-type layer (a_p') in B6TFMO. The subscript "p" refers to the pseudo-cubic index. This calculated value is considerably different to the lattice constant a = 4.785 Å for sapphire (+22.97% lattice mismatch), therefore substrates with similar lattice constants to B6TFMO, namely (100) STO (a = 3.905 Å; lattice mismatch = +0.39%) and (100) LSAT (a = 3.868 Å; lattice mismatch = -0.57%), were selected for subsequent growth experiments employing this two-step process. HR-TEM (**Fig. 1 (a)-(c)**) reveal that these substrates, which allow epitaxial match with the Aurivillius structure, enable growth of continuous ultra-thin Aurivillius phase films. STEM-EDX measurements (**Fig. 1 (d)-(e)**) demonstrate that, as desired, these films are comprised of Bi, Ti, Fe, Mn and O, thus they will be referred to as "BTFMO" films. By utilizing two hundred injections during growth, 16-18 nm BTFMO films were achieved (**Fig. S3, Fig. 1 (g)**) and with one hundred injection pulses per precursor, 7 nm films were achieved (**Fig. 1**). The latter equates to 1.5unit-cells of the Aurivillius phase structure.

Line section measurements along the [100] direction of TEM images allow for comparison between the atom spacings of the *A*-site atoms of the BTFMO films and the atom spacings of the *A*-site atoms of the substrate. Representative atom spacings along the [100] direction of the substrate (black plot), interface (red plot) and at the top of the BTFMO film (blue plot) are shown in **Fig. 1 (c) Fig. 1 (f), Fig. S3 (a) - (b)**. This analysis demonstrates the clear epitaxial relationship between film and substrate and the influence that the substrate has on the a_p' values of the BTFMO films (Fig. 1 (g)). This epitaxial relationship is preserved even after 3.5 unit-cells distance from the interface (as demonstrated by the 18 nm films in **Fig. S3**).

This DLI-CVD method allows realization of epitaxial thin films, crucial for orientation control and for relating the strain state of the material to its multiferroic properties.

Nevertheless, as Zurbuchen et al.[43] explain, defects related to bismuth volatilization are much more likely to occur in epitaxial films compared with bulk samples. Due to a combination of high crystalline anisotropy and unidirectional growth fronts, structural rearrangement is limited to the surface layers of a growing film, so that inadequate activation energies exist to remedy the structural defects within the film. As bismuth migrates away at 850 °C, the structure crystallographically shears to form out-of-phase boundary (OPB) defects, stacking-fault defects and "zig-zag" defects pertaining to anatase-type intergrowths[44-47], which can act as fast diffusion path for volatilizing bismuth.[43] These defects are discussed in further detail in the Supporting Information section and **Fig. S4**

The uncompensated stoichiometry due to loss of bismuth in the film under the 850 °C anneal step results in phase separation of the Aurivillius composition and ex-solution of at least four types of second phase impurities (see **Fig. S5** and Supporting Information). These tend to solidify above the film onto the film surface and have been identified as (i) the bixbyite $(Mn,Fe)_2O_3$ (cubic Ia-3) phase, (ii) an amorphous phase of the $Bi_xTi_yO_z$ composition, (iii) the spinel $(Mn,Fe)_3O_4$ (cubic space group Fd-3m) phase and (iv) the monoclinic $Bi_2Ti_4O_{11}$ (B2/b) phase.

XRD profiles of BTFMO prepared by the 2-step process (**S6 (a)**) also display the complexity of these samples treated by post-anneal at 850 °C. The m = 5 Aurivillius structure is confirmed, however traces of the bixbyite (2θ = 26.6 °, 35.7 °, 38.3 °; JCPDS 08-0010[48]), spinel (2θ = 35.4°; JCPDS (Joint Committee on Powder Diffraction Standards) 79-0419[49]) and $Bi_2Ti_4O_{11}$ (2θ = 27.1 °, 30.5 °, 38.6 °; JCPDS 72-1820[50]) impurity phases are also evident from the XRD patterns. Direct comparison between compositional surface SEM-EDX measurements of thicker (~100 nm) films grown on c-m sapphire (**Fig. 6 (b)**) and STO (**Fig. S6 (c)**) substrates from the same growth run indicates that these surface impurities are characteristic of films grown on epitaxial substrates only. This reinstates the earlier observations[43] that when bismuth out-diffuses to the film surface, the physical constraints of an underlying lattice-matched substrate offers only a low degree of structural rearrangement when compared with growth on non-epitaxial substrates.

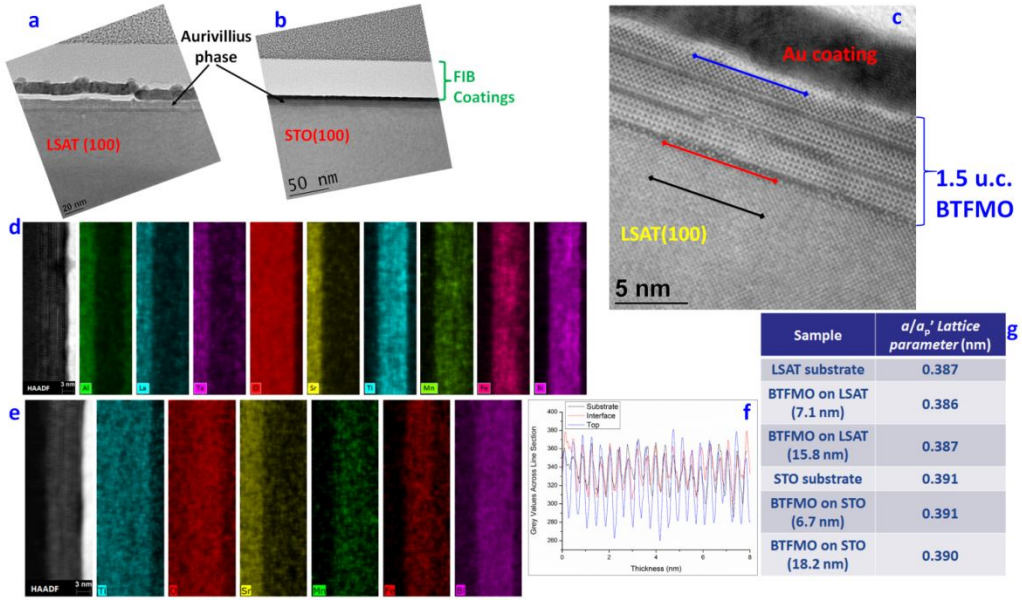
2.2 Single-step process:

The above two-step process was an adaptation of a previous process, successfully employed for thicker films of m = 5 B6TFMO on non-epitaxial substrates, which required deposition of an amorphous film at 630 °C with a subsequent post-anneal at 850 °C in order to surmount the thermodynamic barriers to crystallization. However, temperatures for the growth of epitaxial films are often lower than those needed for bulk synthesis, where crystallization occurs as material is deposited on the surface.[43] Given that there is an enhancement in the diffusion coefficient of bismuth above 710 °C[51], single-step DLI-CVD processes were developed utilizing epitaxial substrates ((100) STO, (100) LSAT and $(001)_p$ NGO (a_p' = 3.858 Å; lattice mismatch = -0.82%) at growth temperatures of 710 °C and 700 °C to investigate if crystallization of the m = 5 phase can be achieved at these lower temperatures, without the need for a subsequent post-anneal. Meanwhile, a lowering of the rate of bismuth diffusion was expected to reduce the issues pertaining to uncompensated stoichiometries and associated structural disorder.

TEM (**Fig. 2 (a) – (b)**) and XRD (**Fig. 2 (c)**) studies demonstrate that decreasing the synthesis temperature significantly increased the phase purity of the films compared with those post-annealed at 850 °C (**Fig. S5**, **Fig. S6 (a)**). Utilizing 100 injections per precursor during the growth process, the 5-layered B6TFMO Aurivillius phases were successfully achieved at 7 nm, or 1.5 unit-cell thicknesses. This single-step growth process on epitaxial substrates enabled the synthesis temperature of B6TFMO to be lowered by 150 °C. Surface SEM-EDX analysis (**Fig. 2 (f)**) confirms the

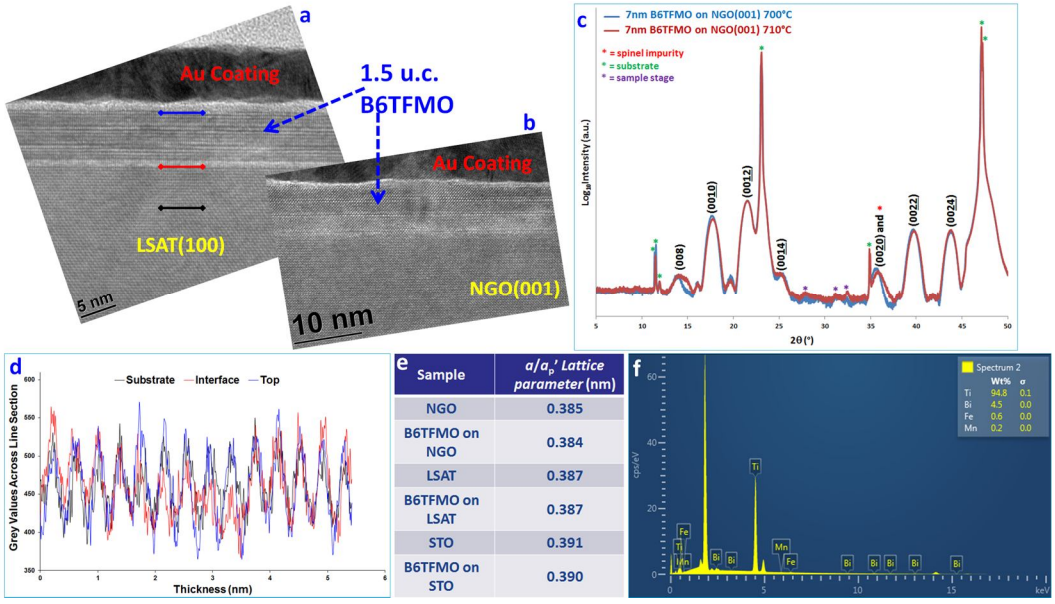
presence of Bi, Fe and Mn in approximately the correct proportions. A substantially higher atomic weight percentage of Ti is observed, as expected from its presence in the underlying STO substrate.

Line section measurements along the [100] direction of TEM data (representative example in **Fig. 2 (a)**) enabled comparison between the atom spacings of the A-site atoms of the B6TFMO films and the atom spacings of the A-site atoms of the substrate. Atom spacings along the [100] direction of the substrate (black plot), interface (red plot), and at the top (bue plot) of the B6TFMO film are displayed in **Fig. 2 (d)**. This analysis demonstrates the 7 nm B6TFMO films are epitaxially matched to the specific substrate used for growth, with the substrate dictating the atom distances within the B6TFMO films (**Fig. 2 (e)**). This epitaxial relationship is preserved throughout the film.



Sample	a/a_p' Lattice parameter (nm)
LSAT substrate	0.387
BTFMO on LSAT (7.1 nm)	0.386
BTFMO on LSAT (15.8 nm)	0.387
STO substrate	0.391
BTFMO on STO (6.7 nm)	0.391
BTFMO on STO (18.2 nm)	0.390

Figure 1. Representative TEM images demonstrating continuous 7 nm Aurivillius phase films prepared by the 2-step DLI-CVD process (post-anneal 850 °C) on **(a), (c)** LSAT (100) and **(b)** STO (100) substrates. STEM-EDX analysis of BTFMO samples on **(d)** LSAT and **(e)** STO confirms Bi, Ti, Fe, Mn and O are successfully incorporated into the 7 nm films prepared by the 2-step DLI-CVD process (post-anneal 850 °C). Line section measurements along the [100] direction of TEM data in **(c)** for substrate (black line), interface (red line) and top of BTFMO film (blue line) are plotted in **(f)** and enable a comparison between lattice parameter of BTFMO film and corresponding substrate, as tabulated in **(g)**.



Sample	a/a_p' Lattice parameter (nm)
NGO	0.385
B6TFMO on NGO	0.384
LSAT	0.387
B6TFMO on LSAT	0.387
STO	0.391
B6TFMO on STO	0.390

Figure 2. Representative TEM images demonstrating continuous 7 nm Aurivillius phase films prepared by the single-step DLI-CVD process (710 °C) on **(a)** LSAT (100) and **(b)** NGO (100) substrates. Line section measurements along the [100] direction of TEM data in **(a)** for substrate (black line), interface (red line) and top of B6TFMO film (blue line) are plotted in **(d)** and enable a comparison between lattice parameter of B6TFMO film and corresponding substrate, as tabulated in **(e)**. **(c)** Representative XRD patterns of B6TFMO on LSAT(100) prepared by the single-step DLI-CVD process at temperatures of 710 and 700 °C demonstrate that the 5-layered B6TFMO Aurivillius phases were successfully achieved at 7 nm thickness. Decreasing the synthesis temperature by 140-150 °C significantly increased the phase purity although presence of the (311) reflection at 2θ ~ 35.4° signifies that precipitation of the spinel $(Mn,Fe)_3O_4$ (cubic space group Fd-3m) phase does however occur at these temperatures. **(f)** Surface SEM-EDX analysis of 7 nm B6TFMO on STO(100) synthesized at 710 °C confirms the presence of Bi, Fe and Mn in approximately the correct proportions.

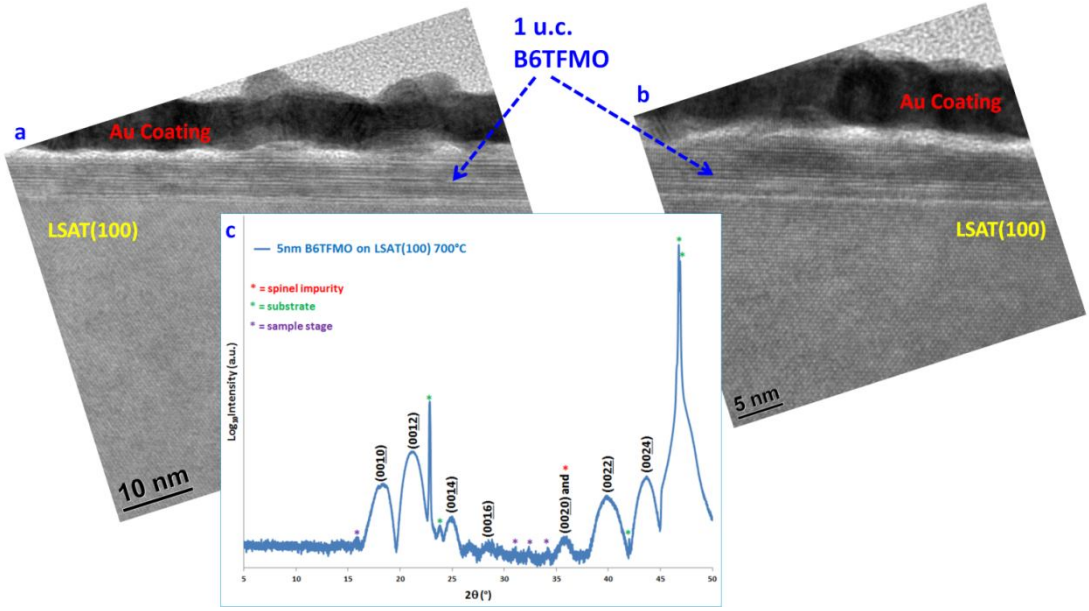


Figure 3. (a), (b) Representative TEM images demonstrating continuous 5 nm Aurivillius phase films prepared by the single-step DLI-CVD process (700 °C) on LSAT (100) substrates. **(c)** Representative XRD pattern demonstrating that the 5-layered B6TFMO Aurivillius phase is successfully achieved at 5 nm thickness (1 unit cell thick B6TFMO). This single-step growth process on epitaxial substrates enabled the synthesis temperature of B6TFMO to be lowered by 150 °C.

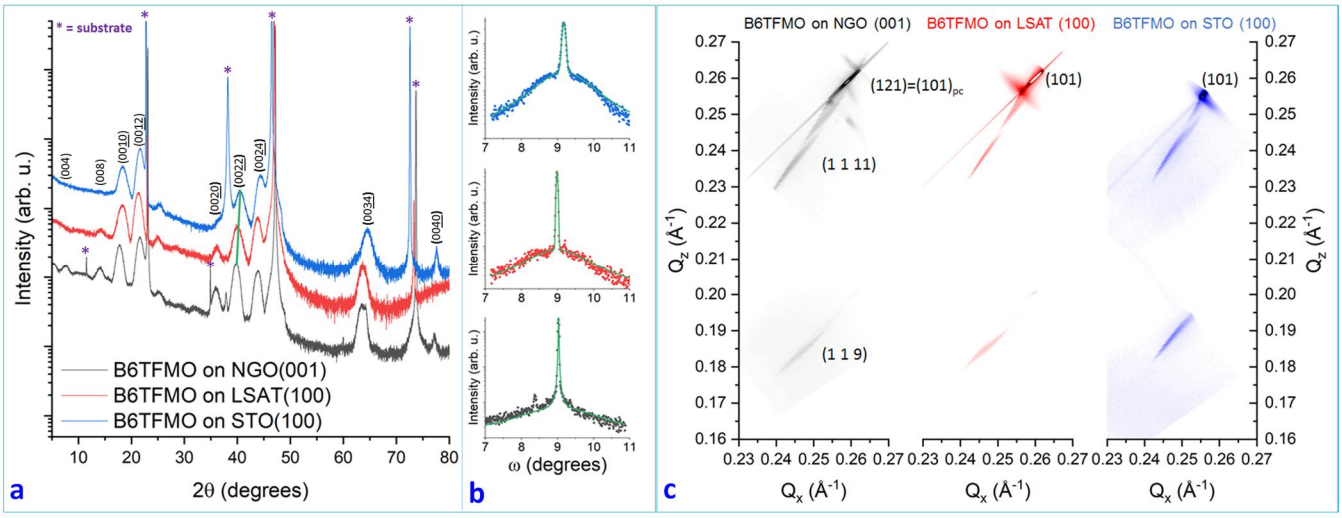


Figure 4. (a) Out-of-plane X-ray diffraction patterns enabling a comparison between 5 nm B6TFMO films grown on NGO, LSAT and STO substrates. **(b)** Rocking curve measurements on the (00$\underline{10}$) Bragg reflections of the films enables assessment of crystal quality. **(c)** The epitaxial relationship between the substrates and the 5 nm B6TFMO films is confirmed using the reciprocal space maps (RSMs) with $[100]_{substrate}//[110]_{film}$ in-plane and $[001]_{substrate}//[001]_{film}$ out-of-plane.

Moreover, by lowering the number of precursor injections during growth to 75, continuous films of 5 nm film thickness, which equates to 1 unit-cell of B6TFMO, were successfully achieved by employing this single-step growth process at the decreased temperature of 700 °C, as observed in representative

TEM (**Fig. 3 (a) – (b)**) and XRD (**Fig. 3 (c)**, **Fig. 4**) studies. Comparative out-of-plane X-ray diffraction patterns obtained from 5 nm films grown on NGO(001), LSAT(100) and STO(100) substrates are shown in **Fig. 4 (a**). The observation of the (00*l*) Bragg reflections indicate a high degree of orientation along the long axis of the structure and the broadening of the peaks (see Supplementary Information) is due to a grain size effect. The shift of the peak position towards higher angle (exemplified by the green line marking the (00$\underline{22}$) reflections in **Fig. 4 (a)**) as the lattice parameter of the substrate increases ($a_{NGO} < a_{LSAT} < a_{STO}$) indicates that the out-of-plane lattice parameter is reducing as expected when tensile strain is applied to a chemical compound, assuming a constant cell volume. The crystal quality was further assessed by measuring rocking curves on the (00$\underline{10}$) Bragg reflections of the films as shown in **Fig. 4 (b)**. The rocking curves present similar features for all substrates with a broad Lorentzian base and a narrow Gaussian component which may indicate the presence of dislocations in the films (see Supplementary information). The rocking curves were fitted with a pseudo-Voigt function and the full width half maximum (FWHM) of the Gaussian (w_G) and Lorentzian (w_L) terms for each sample are summarized in **Table 1**. The film with the narrowest rocking curve is obtained on the NGO(001) substrate.

Table 1. Rocking curve FWHM values for 5 nm B6TFMO films.

	NGO	LSAT	STO
w_G	0.0409(2)	0.0514(2)	0.1035(5)
w_L	1.4(5)	1.8(1)	1.47(3)

The epitaxial relationship between the substrates and the film is confirmed using the RSMs presented in **Fig. 4 (c)** with $[100]_{substrate}//[110]_{film}$ in-plane and $[001]_{substrate}//[001]_{film}$ out-of-plane. The different scattering vector Q_x value between the 5 nm film and substrate indicates that the in-plane lattice parameters of the films are relaxed in each case.

A lowering of the synthesis temperature by 140-150 °C and an associated lowering of the rate of bismuth diffusion significantly reduced the extent of the issues pertaining to uncompensated stoichiometries within the B6TFMO films. We do not observe "zig-zag" defects pertaining to intergrowths of 1-D fragments of anatase-type structures within the B6TFMO films synthesized at 710 and 700 °C. Whereas the majority of the sample is comprised of the m = 5 Aurivillius phase, TEM images (**Fig. S7 (a)**) demonstrate an occasional change in the thickness of the perovskite blocks at specific regions accompanying OPB defects (within the green arrows in **Fig. S7 (a)**) where stacking faults of m = 4 phases form due to their mutual displacements of their interfaces along the c-axis. As discussed above, these types of stacking-fault defects are often seen in the layered Aurivillius phases.[43] While second phase impurities are not completely eliminated for the samples synthesized by the single-step process, they have smaller dimensions (8-40 nm) (**Fig. S 7 (b) – (d)**) compared to those prepared by the two-step process (15-360 nm) (**Fig. S 5**). The volume fraction of surface impurities decreased from 11-12 vol. % to 3-4 vol. % and the root mean square roughness of the films decreased from 8.7-12.4 nm to 1.2-5.3 nm (**Fig. S 7 (d)**). The bixbyite and monoclinic $Bi_2Ti_4O_{11}$ phases which tend to form above 800 °C are not observed for the samples synthesized at 700 and 710 °C. Presence of the (311) reflection at 2θ ~ 35.4° (**Fig. 2 (c)**, **Fig. 3 (c)**) signifies that precipitation of the spinel $(Mn,Fe)_3O_4$ (cubic space group Fd-3m) phase does however occur at these temperatures.[49] Spinel impurity inclusions are visible as speckles both within the Aurivillius phase film (**Fig. S7 (b)**) and on the film surface (**Fig. S7 (c), (d)**). These speckles display d-spacings of 3.0 Å and 2.1 Å corresponding to the (220) and (400) reflections of the spinel phase, respectively.[49,52]

Given that the spinel phases are ferrimagnetic, the presence of these impurities within the samples would complicate any attempts to measure a magnetic signal intrinsic to the main B6TFMO Aurivillius phase. In contrast, these inclusions are not ferroelectric and would not influence the ferroelectric signal. Consequently work was directed towards exploring the ferroelectric properties of these ultra-thin samples.

3. PFM Investigations close to unit-cell thickness:

The critical (or characteristic) size of a ferroelectric has been defined as the minimum physical size below which the ferroelectricity in the material disappears. One source of ferroelectric destabilization at the nano-scale is the formation of polarization induced surface charges induced by the out-of-plane polarization which, if incompletely screened, can produce a depolarization field of magnitude inversely proportional to the thickness of the ferroelectric. This effectively decreases the net out-of-plane ferroelectric polarization, leading to a lack of stability and reproducibility of vertical response at reduced thickness. Below a critical size limit, the electrostatic energy associated with the residual depolarizing field becomes larger than the energy gained by ferroelectric ordering and the out-of-plane polarization vanishes. This critical size limit was previously thought to be 20 nm[53], however significant progress over the last two decades has demonstrated that the ferroelectric critical size limit in thin film materials is much thinner than formerly thought and may be absent in optimized materials.[54,55] Advances in thin film growth techniques have allowed the production of high quality ultra-thin films where epitaxial strain can stabilize symmetry-lowering polar distortions.[56] Epitaxial strain can compensate the adverse influence of thickness reduction and preserve out-of-plane ferroelectricity in ultra-thin ferroelectric films by enabling the spontaneous formation of small ferroelectric domains of alternating polarity to neutralize surface charges and the associated depolarization field, e.g. 4 nm (10 unit-cells (u.c.)) $Pb(Zr_{0.2}Ti_{0.8})O_3$[57] and 1.2 nm (3 u.c.) $PbTiO_3$[58]. In addition, 'strain tuning' can lead to a significant enhancement of the out-of-plane spontaneous polarization in perovskites (e.g. 1nm $BaTiO_3$)[59] and 'confinement strain' aids distortion into the polar orthorhombic phase of fluorite thin films, where surface-energy-driven size effects actually favor polar distortions as thickness is reduced (e.g. 1 nm (2 u.c.) $Hf_{0.8}Zr_{0.2}O_2$)[55]. While effective screening from ionic displacements of the bottom oxide electrode and screening charges at the interface and top surface are believed to aid stabilization of switchable vertical polar states at atomic thickness in 2 u.c. thick $BiFeO_3$.[54]

Devices based on in-plane tunnel junctions would not be hindered by competing depolarization fields upon scaling down to ultra-thin dimensions, meaning that higher ON:OFF tunneling current ratios can be achieved with non-destructive read operations. So far, no such in-plane devices exist in

practice, only device concepts based on theoretical simulations of monochalcogenides have been proposed.[29-32] Reproducibility of RT ferroelectric properties has not yet been validated for ultra-thin monochalcogenides that can be synthesized by scalable growth methods.[32] On the other hand, in-plane ferroelectricity at Curie temperatures above 650°C is established for the Aurivillius phases. Crystal symmetry dictates the major polar axis of the Aurivillius phases lies in-plane,[60] therefore they demonstrate much greater ferroelectric polarization in-plane (P_S up to 50 μC/cm^2) compared with the out-of-plane (P_S of 4 μC/cm^2) direction.[19,22] Gradauskaite *et al*.[61] demonstrated uniaxial in-plane switching behavior in 0.5 u.c. thick films and endurance after 10^{10} switching cycles for 2.5 u.c. thick films of Aurivillius phase $Bi_5Ti_3FeO_{15}$ (m = 4) prepared by pulsed laser deposition. As such, optimized Aurivillius phases at ultra-low thickness are perfect candidates for application as in-plane ferroelectric tunnel junction devices. Moreover, multiferroic tunnel junctions based on the manganese-containing B6TFMO system offer the prospect of producing eight-state information storage based on simultaneous magnetoresistance and electroresistance.[33] The focus of this investigation therefore is to determine whether ferroelectricity persists in B6TFMO at sub-10 nm thicknesses required for technologically competitive multiferroic applications.

Ferroelectric measurements of ultra-thin films can be experimentally challenging. Whereas polarization versus electric-field (P–E) measurements enabled measurements of ferroelectric polarization in previously-grown 100 nm thick samples (in-plane P_s >26 μC/cm^2),[19] these measurements are made difficult by leakage currents when the thickness decreases below a few tens of nanometers. Indications of a polar state may be deduced from diffraction studies, but to demonstrate the existence of a switchable polarization at nano-scale, PFM is the technique of preference.[62]

There has been considerable progress in PFM instrumentation over the last two decades and the DART-PFM technique was utilized in this study to investigate the electromechanical properties of the sub-10 nm manganese containing BTFMO/B6TFMO samples. This technique is designed to boost the piezo signal-to-noise ratio and minimize topographical 'cross-talk', enabling measurements of piezoresponse using probing AC drive amplitudes (V_{AC}) of 3.0 V_{AC} and below (typically 1.0 V_{AC} in this work). The use of minimum as possible V_{AC} is critical for ultra-thin films, where increased biases can result in dielectric breakdown and physical degradation of the surface of nanoscale structures.[22,63] PFM imaging of similar sample areas by VPFM (vertical PFM) and LPFM (lateral PFM) allows complementary mapping of the normal component of the piezoresponse vector and the transversal component of the in-plane piezoresponse (perpendicular to the cantilever axis), respectively. As the PFM tip scans the material surface with a probing signal, V_{AC}, the material responds with a volume change directly linked to its piezoelectric constant, represented by the amplitude images signifying the strength of the electromechanical response. The phase images display the direction of the polarization, where a 180° phase differential represents oppositely orientated domains.

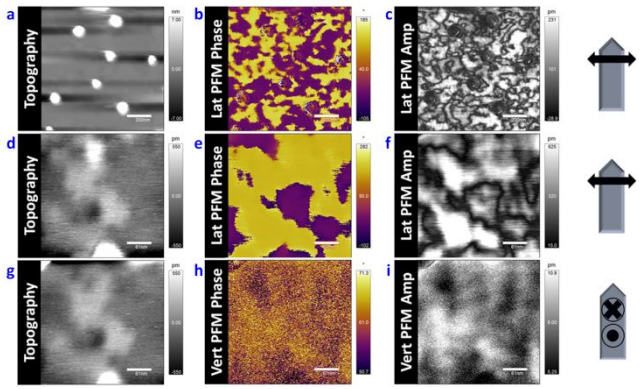


Figure 5 DART-PFM images of 7 nm BTFMO on LSAT (100) prepared by the 2-step process (post-anneal 850 °C). **(a)**, **(d)**, **(g)** Topography, **(b)**, **(e)** lateral (Lat) PFM phase, **(h)** vertical (vert) PFM phase, **(c)**, **(f)** lateral PFM amplitude (amp) and **(i)** vertical PFM amplitude images demonstrating the persistence of ferroelectricity at 1.5 u.c. BTFMO. The direction of motion of the PFM cantilever as it scans the sample surface is indicated to the right of the images.

In-plane ferroelectric domains are clearly observed in the LPFM images (**Fig. 5 (a) – (f)**) for the 1.5 u.c. thick BTFMO films prepared by the two-step process (with post-anneal at 850 °C), whereas a relatively weaker response is observed in the out-of-plane direction (VPFM images, **Fig. 5 (g) – (i)**). Grey areas of intermediate amplitude intensity are consistent with a weak out-of-plane component in **Fig. 5 (i)**. This observation is expected, as the crystal symmetry of the *m*=5 Aurivillius phases, having an odd *m* number of perovskite units, dictates that the polarization primarily lies along the *a*/*b* plane (in-plane, lateral direction), with only minor polarization along the c-axis (out-of-plane, vertical direction).[60] These 7 nm (1.5 u.c. thick) BTFMO films are naturally self-polarized and a random mixture of domain states is exhibited, separated by 180° degree domain walls. Zero amplitude and a noisy phase contrast are observed for the secondary-phase impurities (**Fig. 5 (b) – (c)**), indicating that these phases are not ferroelectric and do not contribute a ferroelectric signal. These impurities and microstructural defects can however influence domain wall activity in the ferroelectric BTFMO thin film, and may *decrease* coercivity by serving as nucleation sites for reverse domains or may *increase* coercivity by contributing to "pinning effects" which can have resistance to domain wall motion.[64] Notwithstanding, Zhang *et al*.[65] reported that defects can be exploited in a positive manner and demonstrated that the increased activation field for domain wall movement caused by pinning defects in tetragonal-like $BiFeO_3$ enabled a 2000% increase in polarization retention compared to best values for previously reported ferroelectric materials.

The domains become smaller and the density of the domains increases with the decrease of processing temperature for the B6TFMO films prepared by the single-step DLI-CVD process (710 °C and 700 °C) (representative examples in **Fig. S 8**).

In PFM imaging of ultra-thin films, it is prudent to consider whether non-ferroelectric mechanisms may contribute to the PFM signal. Under ambient conditions, where the water meniscus persists at the tip-sample junction, voltage-stress-induced electrochemical effects may contribute to the observed response and the water meniscus may affect the tip-sample capacitance and the shape and size of the effective tip-sample contact area during image formation in PFM.[66,67] To

investigate this, comparative PFM experiments were performed at RT and by maintaining the sample at 120 °C on a sample stage with integrated temperature control. Note that this temperature is well below the sample ferroelectric Curie temperature of 700 °C,[68] therefore assessment of ferroelectric endurance was not the focus of these experiments. Rather, evaporation of the wetting water layer is expected at 120 °C, therefore imaging at this temperature enables assessment of whether the presence of water facilitates image formation in PFM. Similarity in response, domain sizes and domain shape between RT measurements (representative examples in **Fig. S 8 (a) – (c)**) and experiments conducted where the sample was maintained at 120 °C over a 3.5 hour time-period is observed (**Fig. S 8 (d) – (f)**). These temperature studies therefore largely exclude a water-mediated mechanism being involved in the PFM image formation.

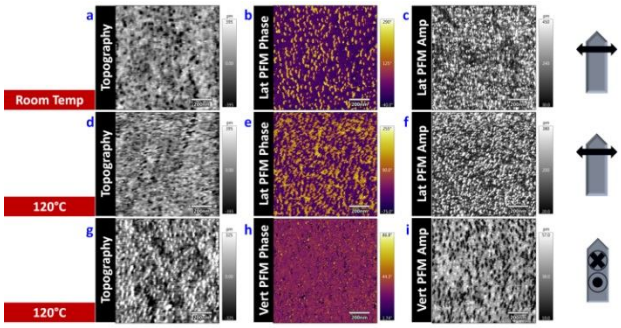


Figure 6. DART-PFM images of 5 nm B6TFMO on NGO (001) prepared by the 1-step process (700 °C). **(a)**, **(b)**, **(c)** Room temperature topography, lateral (lat) PFM phase and lateral PFM amplitude (amp) images, respectively. **(d)**, **(e)**, **(f)** Topography, lateral PFM phase and lateral PFM amplitude images, respectively, where the B6TFMO sample was maintained at 120 °C. **(g)**, **(h)**, **(i)** Topography, vertical (vert) PFM phase and vertical PFM amplitude images, respectively, where the B6TFMO sample was maintained at 120 °C. The direction of motion of the PFM cantilever as it scans the sample surface is indicated to the right of the images. These studies demonstrate the persistence of ferroelectricity at 1 u.c. B6TFMO.

This method was used to demonstrate that ferroelectric domains persist in 1 u.c. thick (5 nm) B6TFMO at RT (**Fig. 6 (a) – (c)**) and at 120 °C (**Fig. 6 (d) – (i)**). This persistence of stable ferroelectricity in 2*D* films of B6TFMO at unit-cell thickness, in both in-plane and out-of-plane directions in a multiferroic system, is significant as it opens up possibilities for miniaturizing multiferroic-based devices.

As anticipated from crystal symmetry for Aurivillius phases having odd *m*-values,[69] single-frequency PFM imaging experiments (representative example in **Fig. S9**) demonstrate that all sets of the films are piezoelectric, with expected higher piezoresponses in the lateral direction (22.2, 17.0 and 10.4 pm/V for B6TFMO on STO, LSAT and NGO, respectively) compared with those measured in the vertical direction (4.0, 2.2 and 2.1 pm/V for B6TFMO on STO, LSAT and NGO, respectively). The in-plane piezoelectric coefficient for previously grown non-epitaxial B6TMO (100 nm) on sapphire is 19 pm/V.[18] In this contribution, B6TFMO films on STO(100) are under tensile strain, whereas B6TFMO films on LSAT(100) and NGO (001) are under compressive strain (refer to **Fig. 4**). We note a trend where piezoresponse is enhanced with increase in tensile strain, whereas compressive strain leads to a decrease in piezoresponse for the B6TFMO films This correlates with density functional theory (DFT) predictions of Birenbaum and Ederer.[23] The out-of-plane values are lower than the 100 nm thick B6TFMO films (8 pm/V),[18] which are more randomly orientated compared to the epitaxial films in this work. For non-epitaxial 100 nm thick B6TFMO, some of the *a*-axis oriented grains are tilted out-of-plane, thus contributing to a higher piezoresponse in the vertical direction.[17,18] The out-of-plane responses for the epitaxial B6TFMO films are comparable to values reported for BFO films of similar thickness.[70]

To investigate whether ferroelectricity is anisotropic within the plane, PFM experiments were performed with the cantilever aligned parallel to the [100] substrate direction. This was directly followed by PFM experiments after rotation of the sample by 90° so that the cantilever was aligned parallel to the [010] substrate direction (**Fig. 7** and **Fig. S10**). Experiments demonstrate isotropic random distribution of in-plane domains at 1.5 u.c. and 1 u.c. thicknesses for B6TFMO on STO(100) and LSAT(100). Experiments of B6TFMO on NGO(001) at 1.5 u.c. and 1 u.c. thicknesses (**Fig. 7** and **Fig. S11**) indicate that domains are directed 45° away from the Aurivillius phase polar axis ($[010]_{NGO}$), analogous to studies of BTFO by Gradauskaite *et al.*[61] Although uniaxial in-plane ferroelectric domains are not achieved at thicknesses of 1 u. c. and above,[61] future studies will assess the potential for NGO(001) to provide sufficient substrate lattice mismatch to potentially stabilize uniaxial ferroelectric anisotropy in thinner (0.5 u.c.) B6TFMO films.

As a PFM tip scans a material surface with an applied DC bias, V_{DC}, it leaves a trailing field which can generate an in-plane electric field.[27,61,71-73] PFM lithography can be used to modify the ferroelectric polarization of the sample through the application of the DC bias and enables domain arrays and complex patterns to be "written" without changing the surface topography. By starting from an unpoled condition, then by aligning the polarization of the B6TFMO films underneath the tip to this trailing field direction, lateral switching and reversal of the ferroelectric domains can be achieved (**Fig. 8**). With application of +5 V_{DC} to the background and by performing PFM lithography using -5 V_{DC} to write "Catalyst", the in-plane components of the electrostatic field produced by the tip results in switching of the in-plane polarization components. A PFM lithography pattern demonstrating anti-parallel polarization states is generated when the surface is re-imaged by a probing signal, V_{AC} (**Fig. 8 (a), (c), (e)**). Despite the presence of defects and secondary phases, domain wall motion was not hindered by possible pinning effects and clear ferroelectric switching was achieved in the lateral direction. We emphasize that the source of the lateral PFM signal in this multiferroic material system is undoubtedly field-induced piezoelectric strain. The fact that the vertical PFM response of the poled areas shows a very weak response in comparison (**Fig. 8 (d), (f)**) would counter an argument that the origin of the PFM signals could have non-ferroelectric electrostatics in origin (e.g. surface charging, trapped charges, oxygen vacancy migration etc.), given that electrostatics, which can either effect the cone of the tip or the cantilever, exert forces in the vertical direction.[27] Electrostatic forces provide minimal contribution to the in-plane response.[72] Thus, we confirm that the lateral PFM signals observed close to unit-cell thickness in this 2*D* multiferroic B6TFMO system are primarily induced by electrically-induced surface displacements due to the converse piezoelectric effect.

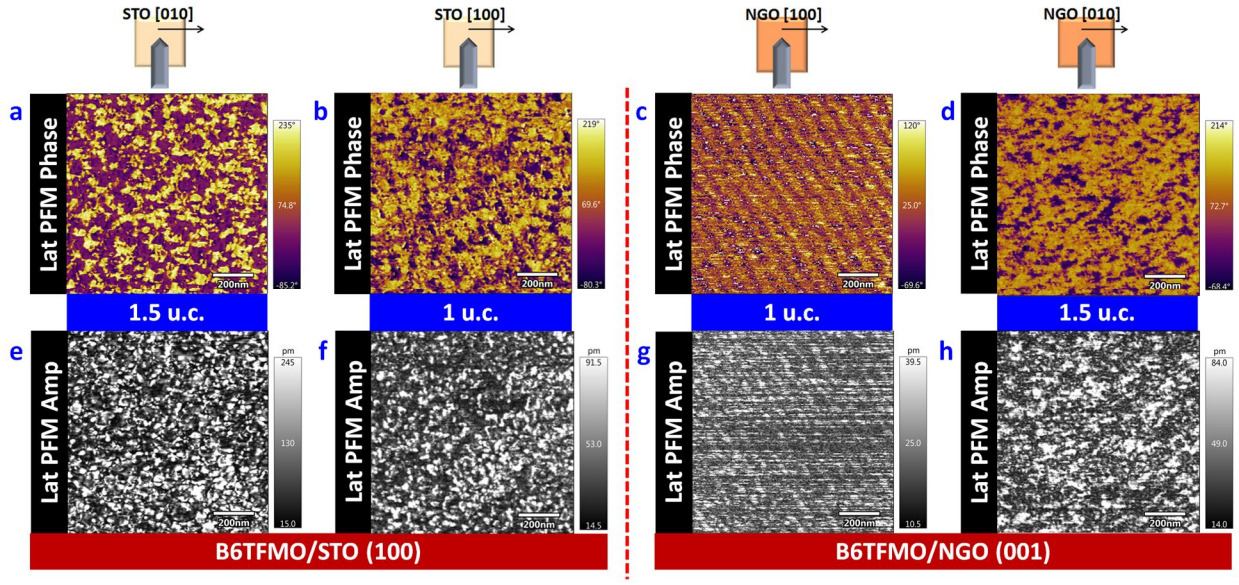


Figure 7. Lateral DART-PFM phase and amplitude (amp) images of 5 nm B6TFMO on STO (100) **(a)**, **(b)**, **(e)**, **(f)** summarising the isotropic random distribution of in-plane domains at 1.5 and 1 unit cell thicknesses. Lateral DART-PFM images of 5 nm B6TFMO on NGO (001) **(c)**, **(d)**, **(g)**, **(h)** indicate that domains are oriented 45° away from the Aurivillius phase polar axis ($[010]_{NGO}$). This observation is more pronounced with decrease in thickness. Images were obtained using a "super sharp" probe (<5 nm tip radius). Images **(a), (e), (d)** and **(h)** were performed with the cantilever scanning direction parallel to the $[010]_{substrate}$ axis. The samples were rotated 90° for images **(b), (f), (c)** and **(g)** where the cantilever scanning direction was parallel to the $[100]_{substrate}$ axis. Uniaxial ferroelectric anisotropy is not observed at 1.5 and 1 unit cell thicknesses for the samples investigated in this contribution.

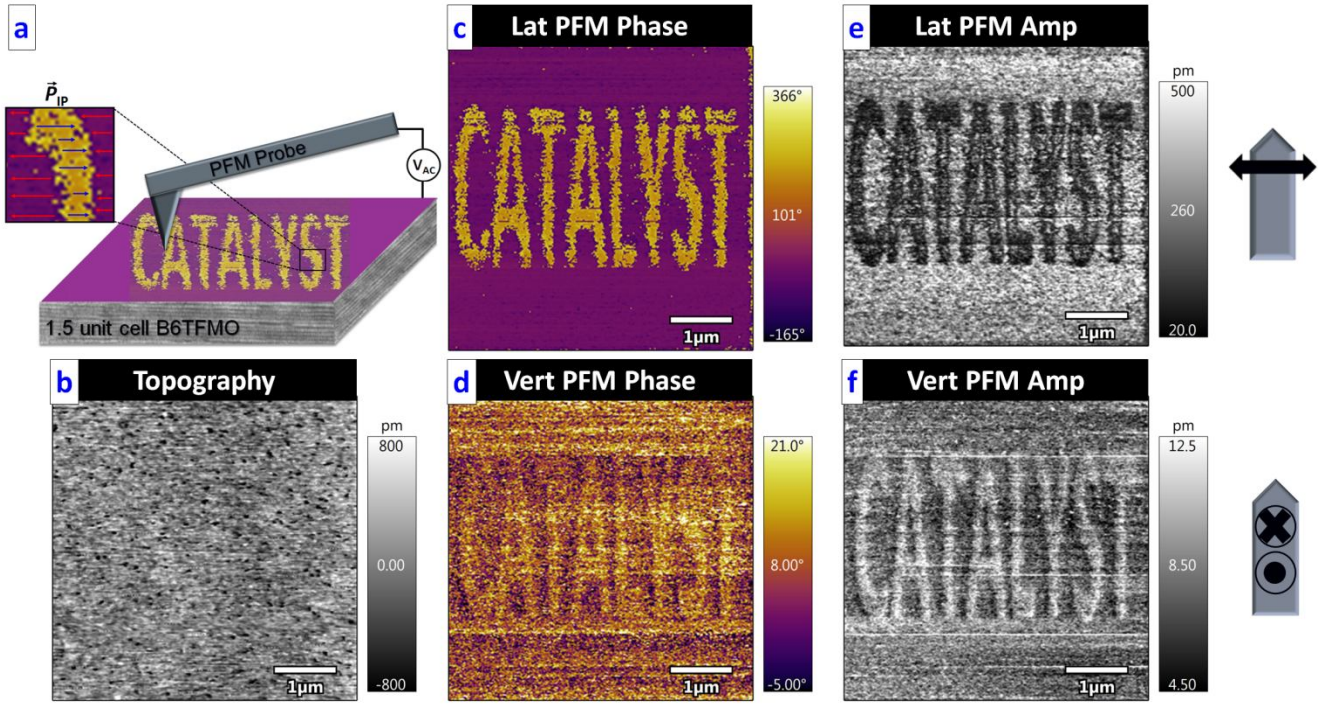


Figure 8. DART-PFM lithography studies of 7 nm B6TFMO on STO (100) prepared by the 1-step process (700 °C). Ferroelectric poling was performed at room temperature with application of +5 V_{DC} to the background and by performing PFM lithography using -5 V_{DC} to write "Catalyst". **(a)** The "read" step was performed with a probing signal (V_{AC}) of 3.0 V. The red and blue arrows within a close-up of a switched area represent the direction of the in-plane polarization (P_{IP}). **(b)** Unchanged sample topography after the ferroelectric poling step. **(c)** Lateral (Lat) PFM phase, **(e)** lateral PFM amplitude (amp), **(d)** vertical (vert) PFM phase, **(f)** vertical PFM amplitude images. The direction of motion of the PFM cantilever as it scans the sample surface is indicated to the right of the figure. These studies demonstrate stable in-plane ferroelectric switching behavior for 1.5 u.c. thick B6TFMO.

CONCLUSIONS: It has been emphasized[20] that a critical requirement for technologically competitive multiferroics is the achievement of RT multiferroic behavior at sub-10 nm length scales. In this contribution, we demonstrate the recent progress in the optimization of multiferroic B6TFMO towards accomplishing this goal. Enhanced single-step DLI-CVD scalable growth processes were developed at 710 °C and 700 °C, enabling a lowering of the synthesis temperature by 150 °C and a significantly reduced level of structural disorder, compared with a two-step process involving post-anneal at 850 °C. The ability to synthesize ultra-thin (<7 nm) 2*D* B6TFMO films which are epitaxially matched to their corresponding substrate offers the prospect of tuning ferroelectric polarization, cation partitioning and magnetic moment by altering epitaxial strain.[23] Thin film quality and sample purity were substantially enhanced for samples synthesized at the lower temperatures, with the volume fraction of surface impurities decreasing from 11-12 % to 3-4 %. We draw attention to the fact that even low levels of impurities can be responsible for the observed ferromagnetic signal in a sample and rigorous analysis of sample purity is required before one can be confident that a material is truly a single-phase multiferroic.[15,17,18,25,26,74,75] Furthermore, although possible domain wall pinning by defects and impurities did not prevent local, PFM switching of lateral ferroelectric domains in B6TFMO, microstructural resistance to domain-wall motion may be an issue for macroscopic ferroelectric and ferromagnetic measurements.[64] Work is underway to eliminate secondary phase impurities to improve ferroelectric switching behavior and to permit assessment of ferromagnetism and magnetoelectric switching in sub-10 nm phase pure B6TFMO films. Here we demonstrate the first direct evidence for the persistence of stable ferroelectric polarization at RT and above in the multiferroic B6TFMO system at unit-cell thickness. The orientation of the ferroelectric polarization can be switched and arrays can be "written" and "read" to demonstrate states which permit anti-parallel information storage in ultra-thin B6TFMO. As expected by crystal symmetry, higher responses are observed in the lateral direction in B6TFMO. In agreement with DFT predictions,[23] piezoresponse is enhanced with increased tensile epitaxial strain. Given that 2D ultra-thin films can be synthesized by scalable growth methods, B6TFMO demonstrates potential for utilization in novel in-plane devices enabling ferroelectric control of tunnel electron resistance. These miniaturized in-plane tunnel junction devices have the significant advantage that performance would not be hindered by competing depolarization fields upon scaling down to ultra-thin dimensions. Data storage devices based on 2*D* single-phase multiferroics would have the ability to produce eight different ('yes' / 'no') logic states.[33] Furthermore, because ferroelectric switching involves domain nucleation and growth, the ability to tailor nucleation-limited ferroelectric domain switching enables the creation of artificial nano-synapses where synaptic strengths evolve depending on the switching pulse amplitude and duration.[76,77] Multiple-levels of 'memristor' states can thus be created by controlling domain evolution. This multivalued logic will allow data processing using not only 'yes' and 'no', but also 'either yes or no' or 'maybe' operations, thus serving as unique memory elements in future neuromorphic computing systems.[78]

ASSOCIATED CONTENT

Supporting Information. A schematic of a five-layered Aurivillius phase structure and additional electron microscopy, X-ray diffraction and scanning probe microscopy images are included to support the study. Detail on the types of defects and impurity phases generated in the samples prepared by the 2-step process (850 °C post-anneal) is provided. This material is available free of charge via the Internet at http://pubs.acs.org.

AUTHOR INFORMATION

Corresponding Author

* lynette.keeney@tyndall.ie

Author Contributions

L.K. conceived and coordinated the project. L.K. developed the DLI-CVD processes, synthesized the BTFMO and B6TFMO thin films, performed AFM and PFM characterization and interpreted the results, in discussion with the other authors. M.S. performed FIB cross-sectioning of lamellae for TEM and performed HR-SEM, SEM-EDX and HR-TEM analysis of the BTFMO and B6TFMO thin films. Z.S. performed probe-corrected HAADF-STEM and STEM-EXD characterization of the BTFMO films. M.O'S. and J. A. performed XRD analysis, rocking curve measurements and reciprocal space mapping of the 5 nm B6TFMO films. L.C. performed XRD characterization of the 7 nm and 5 nm BTFMO and B6TFMO films. L.K. wrote the first draft of the manuscript. The final version of the manuscript was written through contributions of all authors. All authors have given approval to the final version of the manuscript.

Funding Sources

This publication has emanated from research conducted with the financial support of the Royal Society-Science Foundation Ireland University Research Fellowship UF 140263 and Enhancement Award RGF\EA\180206. Research reported in this publication was supported by the Royal Irish Academy / Royal Society International Exchange Cost-Share Programme 2019. The XRD facility used at University of Liverpool was supported by EPSRC (Grant EP/P001513/1). This work was partially supported by the Horizon 2020 ASCENT EU project (Access to European Nanoelectronics Network - Project no. 654384) and a Tyndall National Institute Catalyst Award (4881/R18549).

ACKNOWLEDGMENT

This publication has emanated from research conducted with the financial support of the Royal Society-Science Foundation Ireland University Research Fellowship UF 140263 and Enhancement Award RGF\EA\180206. Research reported in this publication was supported by the Royal Irish Academy / Royal Society International Exchange Cost-Share Programme 2019. The XRD facility used at University of Liverpool was supported by EPSRC (Grant EP/P001513/1). This work was partially supported by the Horizon 2020 ASCENT EU project (Access to European Nanoelectronics Network - Project no. 654384) and a Tyndall National Institute Catalyst Award (4881/R18549). We thank Ivana Savić, Giorgos Fagas, Emanuele Pelucchi, Michael Nolan and Ray Duffy for critical reading of this manuscript.

REFERENCES

(1) Manipatruni, S.; Nikonov, D. E.; Young, I. A. Beyond CMOS computing with spin and polarization. *Nature Physics* **2018**, *14*, 338-343.

(2) Manipatruni, S.; Nikonov, D. E.; Lin, C.-C.; Gosavi, T. A.; Liu, H.; Prasad, B.; Huang, Y.-L.; Bonturim, E.; Ramesh, R.; Young, I. A. Scalable energy-efficient magnetoelectric spin–orbit logic. *Nature* **2019**, *565*, 35-42.

(3) Gajek, M.; Bibes, M.; Fusil, S.; Bouzehouane, K.; Fontcuberta, J.; Barthelemy, A.; Fert, A. Tunnel junctions with multiferroic barriers. *Nat Mater* **2007**, *6*, 296-302.

(4) Katayama, T.; Yasui, S.; Hamasaki, Y.; Shiraishi, T.; Akama, A.; Kiguchi, T.; Itoh, M. Ferroelectric and Magnetic Properties in Room-Temperature Multiferroic GaxFe2−xO3 Epitaxial Thin Films. *Advanced Functional Materials* **2018**, *28*, 1704789.

(5) Evans, D. M.; Schilling, A.; Kumar, A.; Sanchez, D.; Ortega, N.; Arredondo, M.; Katiyar, R. S.; Gregg, J. M.; Scott, J. F. Magnetic switching of ferroelectric domains at room temperature in multiferroic PZTFT. *Nature Communications* **2013**, *4*, 1534.

(6) Mandal, P.; Pitcher, M. J.; Alaria, J.; Niu, H.; Borisov, P.; Stamenov, P.; Claridge, J. B.; Rosseinsky, M. J. Designing switchable polarization and magnetization at room temperature in an oxide. *Nature* **2015**, *525*, 363-366.

(7) Jia, T.; Fan, Z.; Yao, J.; Liu, C.; Li, Y.; Yu, J.; Fu, B.; Zhao, H.; Osada, M.; Esfahani, E. N.; Yang, Y.; Wang, Y.; Li, J.-Y.; Kimura, H.; Cheng, Z. Multifield Control of Domains in a Room-Temperature Multiferroic 0.85BiTi0.1Fe0.8Mg0.1O3–0.15CaTiO3 Thin Film. *ACS Applied Materials & Interfaces* **2018**, *10*, 20712-20719.

(8) Liu, C.; An, F.; Gharavi, P. S. M.; Lu, Q.; Zha, J.; Chen, C.; Wang, L.; Zhan, X.; Xu, Z.; Zhang, Y.; Qu, K.; Yao, J.; Ou, Y.; Zhao, Z.; Zhong, X.; Zhang, D.; Valanoor, N.; Chen, L.; Zhu, T.; Chen, D.; Zhai, X.; Gao, P.; Jia, T.; Xie, S.; Zhong, G.; Li, J. Large-scale multiferroic complex oxide epitaxy with magnetically switched polarization enabled by solution processing. *National Science Review* **2019**, *7*, 84-91.

(9) Wang, J.; Neaton, J. B.; Zheng, H.; Nagarajan, V.; Ogale, S. B.; Liu, B.; Viehland, D.; Vaithyanathan, V.; Schlom, D. G.; Waghmare, U. V.; Spaldin, N. A.; Rabe, K. M.; Wuttig, M.; Ramesh, R. Epitaxial BiFeO₃ Multiferroic Thin Film Heterostructures. *Science* **2003**, *299*, 1719-1722.

(10) Lee, H. N.; Hesse, D.; Zakharov, N.; Gösele, U. Ferroelectric Bi_{3.25}La_{0.75}Ti₃O₁₂ Films of Uniform a-Axis Orientation on Silicon Substrates. *Science* **2002**, *296*, 2006-2009.

(11) Wouters, D. J.; Maes, D.; Goux, L.; Lisoni, J. G.; Paraschiv, V.; Johnson, J. A.; Schwitters, M.; Everaert, J.-L.; Boullart, W.; Schaekers, M.; Willegems, M.; Vander Meeren, H.; Haspeslagh, L.; Artoni, C.; Caputa, C.; Casella, P.; Corallo, G.; Russo, G.; Zambrano, R.; Monchoix, H.; Vecchio, G.; Van Autryve, L. Integration of SrBi2Ta2O9 thin films for high density ferroelectric random access memory. *Journal of Applied Physics* **2006**, *100*, -.

(12) Park, B. H.; Kang, B. S.; Bu, S. D.; Noh, T. W.; Lee, J.; Jo, W. Lanthanum-substituted bismuth titanate for use in non-volatile memories. *Nature* **1999**, *401*, 682-684.

(13) Fujii, E.; Uchiyama, K. First 0.18 μm SBT-Based Embedded FeRAM Technology with Hydrogen Damage Free Stacked Cell Structure. *Integrated Ferroelectrics* **2003**, *53*, 317-323.

(14) Scott, J. F. Room-temperature multiferroic magnetoelectrics. *NPG Asia Mater* **2013**, *5*, e72.

(15) Schmidt, M.; Amann, A.; Keeney, L.; Pemble, M. E.; Holmes, J. D.; Petkov, N.; Whatmore, R. W. Absence of Evidence ≠ Evidence of Absence: Statistical Analysis of Inclusions in Multiferroic Thin Films. *Scientific Reports* **2014**, *4*, 5712.

(16) Keeney, L.; Downing, C.; Schmidt, M.; Pemble, M. E.; Nicolosi, V.; Whatmore, R. W. Direct atomic scale

determination of magnetic ion partition in a room temperature multiferroic material. *Scientific Reports* **2017**, *7*, 1737.

(17) Faraz, A.; Maity, T.; Schmidt, M.; Deepak, N.; Roy, S.; Pemble, M. E.; Whatmore, R. W.; Keeney, L. Direct visualization of magnetic-field-induced magnetoelectric switching in multiferroic aurivillius phase thin films. *Journal of the American Ceramic Society* **2017**, *100*, 975-987.

(18) Keeney, L.; Maity, T.; Schmidt, M.; Amann, A.; Deepak, N.; Petkov, N.; Roy, S.; Pemble, M. E.; Whatmore, R. W. Magnetic Field-Induced Ferroelectric Switching in Multiferroic Aurivillius Phase Thin Films at Room Temperature. *Journal of the American Ceramic Society* **2013**, *96*, 2339-2357.

(19) Faraz, A.; Ricote, J.; Jimenez, R.; Maity, T.; Schmidt, M.; Deepak, N.; Roy, S.; Pemble, M. E.; Keeney, L. Exploring ferroelectric and magnetic properties of Tb-substituted m = 5 layered Aurivillius phase thin films. *Journal of Applied Physics* **2018**, *123*, 124101.

(20) Spaldin, N. A.; Ramesh, R. Advances in magnetoelectric multiferroics. *Nature Materials* **2019**, *18*, 203-212.

(21) Li, S.; Eastman, J. A.; Li, Z.; Foster, C. M.; Newnham, R. E.; Cross, L. E. Size effects in nanostructured ferroelectrics. *Physics Letters A* **1996**, *212*, 341-346.

(22) Keeney, L.; Smith, R. J.; Palizdar, M.; Schmidt, M.; Bell, A. J.; Coleman, J. N.; Whatmore, R. W. Ferroelectric Behavior in Exfoliated 2D Aurivillius Oxide Flakes of Sub-Unit Cell Thickness. *Advanced Electronic Materials* **2020**, *6*, 1901264.

(23) Birenbaum, A. Y.; Ederer, C. Controlling the cation distribution and electric polarization with epitaxial strain in Aurivillius-phase Bi5FeTi3O15. *Applied Physics Letters* **2016**, *108*, 082903.

(24) Alexe, M.; Scott, J. F.; Curran, C.; Zakharov, N. D.; Hesse, D.; Pignolet, A. Self-patterning nano-electrodes on ferroelectric thin films for gigabit memory applications. *Applied Physics Letters* **1998**, *73*, 1592-1594.

(25) Keeney, L.; Kulkarni, S.; Deepak, N.; Schmidt, M.; Petkov, N.; Zhang, P. F.; Cavill, S.; Roy, S.; Pemble, M. E.; Whatmore, R. W. Room temperature ferroelectric and magnetic investigations and detailed phase analysis of Aurivillius phase Bi5Ti3Fe0.7Co0.3O15 thin films. *Journal of Applied Physics* **2012**, *112*, 052010.

(26) Palizdar, M.; Comyn, T. P.; Ward, M. B.; Brown, A. P.; Harrington, J. P.; Kulkarni, S.; Keeney, L.; Roy, S.; Pemble, M. E.; Whatmore, R. W.; Quinne, C.; Kilcoyne, S. H.; Bell, A. J. Crystallographic and Magnetic Identification of Secondary Phase in Oriented Bi5Fe0.5Co0.5Ti3O15 Ceramics. *Journal of Applied Physics* **2012**, *112*, 073919.

(27) Vasudevan, R. K.; Matsumoto, Y.; Cheng, X.; Imai, A.; Maruyama, S.; Xin, H. L.; Okatan, M. B.; Jesse, S.; Kalinin, S. V.; Nagarajan, V. Deterministic arbitrary switching of polarization in a ferroelectric thin film. *Nature Communications* **2014**, *5*, 4971.

(28) Denev, S. A.; Lummen, T. T. A.; Barnes, E.; Kumar, A.; Gopalan, V. Probing Ferroelectrics Using Optical Second Harmonic Generation. *Journal of the American Ceramic Society* **2011**, *94*, 2699-2727.

(29) Shen, X.-W.; Fang, Y.-W.; Tian, B.-B.; Duan, C.-G. Two-Dimensional Ferroelectric Tunnel Junction: The Case of Monolayer In:SnSe/SnSe/Sb:SnSe Homostructure. *ACS Applied Electronic Materials* **2019**, *1*, 1133-1140.

(30) Chang, K.; Liu, J.; Lin, H.; Wang, N.; Zhao, K.; Zhang, A.; Jin, F.; Zhong, Y.; Hu, X.; Duan, W.; Zhang, Q.; Fu, L.; Xue, Q.-K.; Chen, X.; Ji, S.-H. Discovery of robust in-plane ferroelectricity in atomic-thick SnTe. *Science* **2016**, *353*, 274-278.

(31) Liu, J.; Chang, K.; JI, S.-H.; Chen, X.; Fu, L. Apparatus and methods for memory using in-plane polarization.

(32) Shen, H.; Liu, J.; Chang, K.; Fu, L. In-Plane Ferroelectric Tunnel Junction. *Physical Review Applied* **2019**, *11*, 024048.

(33) Yang, F.; Tang, M. H.; Ye, Z.; Zhou, Y. C.; Zheng, X. J.; Tang, J. X.; Zhang, J. J.; He, J. Eight logic states of tunneling magnetoelectroresistance in multiferroic tunnel junctions. *Journal of Applied Physics* **2007**, *102*, 044504.

(34) Weber, U.; Schumacher, M.; Lindner, J.; Boissière, O.; Lehnen, P.; Miedl, S.; Baumann, P. K.; Barbar, G.; Lohe, C.; McEntee, T. AVD® technology for deposition of next generation devices. *Microelectronics Reliability* **2005**, *45*, 945-948.

(35) Zhang, P. F.; Deepak, N.; Keeney, L.; Pemble, M. E.; Whatmore, R. W. The structural and piezoresponse properties of c-axis-oriented Aurivillius phase Bi5Ti3FeO15 thin films deposited by atomic vapor deposition. *Applied Physics Letters* **2012**, *101*, -.

(36) Faraz, A.; Deepak, N.; Schmidt, M.; Pemble, M. E.; Keeney, L. A study of the temperature dependence of the local ferroelectric properties of c-axis oriented Bi6Ti3Fe2O18 Aurivillius phase thin films: Illustrating the potential of a novel lead-free perovskite material for high density memory applications. *AIP Advances* **2015**, *5*, 087123.

(37) Rodriguez, B. J.; Callahan, C.; Kalinin, S. V.; Proksch, R. Dual-frequency resonance-tracking atomic force microscopy. *Nanotechnology* **2007**, *18*, 475504.

(38) Hong, S.; Woo, J.; Shin, H.; Jeon, J. U.; Pak, Y. E.; Colla, E. L.; Setter, N.; Kim, E.; No, K. Principle of ferroelectric domain imaging using atomic force microscope. *Journal of Applied Physics* **2001**, *89*, 1377-1386.

(39) Kalinin, S. V.; Rodriguez, B. J.; Jesse, S.; Shin, J.; Baddorf, A. P.; Gupta, P.; Jain, H.; Williams, D. B.; Gruverman, A. Vector Piezoresponse Force Microscopy. *Microscopy and Microanalysis* **2006**, *12*, 206-220.

(40) Armstrong, R. A.; Newnham, R. E. Bismuth titanate solid solutions. *Materials Research Bulletin* **1972**, *7*, 1025-1034.

(41) Suárez, D. Y.; Reaney, I. M.; Lee, W. E. Relation between tolerance factor and Tc in Aurivillius compounds. *Journal of Materials Research* **2011**, *16*, 3139-3149.

(42) Shannon, R. D. Revised effective ionic radii and systematic studies of interatomic distances in halides and chalcogenides. *Acta Crystallographica Section A* **1976**, *32*, 751-767.

(43) Zurbuchen, M. A.; Tian, W.; Pan, X. Q.; Fong, D.; Streiffer, S. K.; Hawley, M. E.; Lettieri, J.; Jia, Y.; Asayama, G.; Fulk, S. J.; Comstock, D. J.; Knapp, S.; Carim, A. H.; Schlom, D. G. Morphology, structure, and nucleation of out-of-phase boundaries (OPBs) in epitaxial films of layered oxides. *Journal of Materials Research* **2007**, *22*, 1439-1471.

(44) Batuk, D.; Tsirlin, A. A.; Filimonov, D. S.; Zakharov, K. V.; Volkova, O. S.; Vasiliev, A.; Hadermann, J.; Abakumov, A. M. Bi3n+1Ti7Fe3n−3O9n+11 Homologous Series: Slicing Perovskite Structure with Planar Interfaces Containing Anatase-like Chains. *Inorganic Chemistry* **2016**, *55*, 1245-1257.

(45) Batuk, D.; Batuk, M.; Filimonov, D. S.; Zakharov, K. V.; Volkova, O. S.; Vasiliev, A. N.; Tyablikov, O. A.; Hadermann, J.; Abakumov, A. M. Crystal Structure, Defects, Magnetic and Dielectric Properties of the Layered Bi3n+1Ti7Fe3n−3O9n+11 Perovskite-Anatase Intergrowths. *Inorganic Chemistry* **2017**, *56*, 931-942.

(46) MacLaren, I.; Wang, L.; Craven, A. J.; Ramasse, Q. M.; Schaffer, B.; Kalantari, K.; Reaney, I. M. The atomic structure and chemistry of Fe-rich steps on antiphase boundaries in Ti-doped Bi0.9Nd0.15FeO3. *APL Materials* **2014**, *2*, 066106.

(47) Liu, Y.; Zhu, Y.-L.; Tang, Y.-L.; Wang, Y.-J.; Li, S.; Zhang, S.-R.; Han, M.-J.; Ma, J.-Y.; Suriyaprakash, J.; Ma, X.-L. Controlled Growth and Atomic-Scale Mapping of Charged Heterointerfaces in PbTiO3/BiFeO3 Bilayers. *ACS Applied Materials & Interfaces* **2017**, *9*, 25578-25586.

(48) Fleischer, M.; Richmond, W. E. The manganese oxide minerals, a preliminary report. *Economic Geology* **1943**, *38*, 269−286.

(49) Fleet, M. E. The structure of magnetite: Symmetry of cubic spinels. *Journal of Solid State Chemistry* **1986**, *62*, 75-82.

(50) Petushkova, L. V.; Dmitrieva, S. P.; Pobedimskaya, E. A.; Belov, N. B. Crystalline structure of Bi2Ti4O11. *Doklady Akademii Nauk SSSR* **1974**, *216*, 544-546.

(51) Palkar, G. D.; Sitharamarao, D. N.; Dasgupta, A. K. Self-diffusion of bismuth in bismuth oxide. *Transactions of the Faraday Society* **1963**, *59*, 2634-2638.

(52) Lick, I. D.; Soria, D. B. SYNTHESIS OF MnFeO3 FROM THE OXIDATIVE THERMAL DECOMPOSITION OF Mn(Fe(CN)5NO)·2H2O. *Journal of the Argentine Chemical Society* **2009**, *97*, 102-108.

(53) Li, S.; Eastman, J. A.; Vetrone, J. M.; Foster, C. M.; Newnham, R. E.; Cross, L. E. Dimension and Size Effects in Ferroelectrics. *Japanese Journal of Applied Physics* **1997**, *36*, 5169-5174

(54) Wang, H.; Liu, Z. R.; Yoong, H. Y.; Paudel, T. R.; Xiao, J. X.; Guo, R.; Lin, W. N.; Yang, P.; Wang, J.; Chow, G. M.; Venkatesan, T.; Tsymbal, E. Y.; Tian, H.; Chen, J. S. Direct observation of room-temperature out-of-plane ferroelectricity and tunneling electroresistance at the two-dimensional limit. *Nature Communications* **2018**, *9*, 3319.

(55) Cheema, S. S.; Kwon, D.; Shanker, N.; dos Reis, R.; Hsu, S.-L.; Xiao, J.; Zhang, H.; Wagner, R.; Datar, A.; McCarter, M. R.; Serrao, C. R.; Yadav, A. K.; Karbasian, G.; Hsu, C.-H.; Tan, A. J.; Wang, L.-C.; Thakare, V.; Zhang, X.; Mehta, A.; Karapetrova, E.; Chopdekar, R. V.; Shafer, P.; Arenholz, E.; Hu, C.; Proksch, R.; Ramesh, R.; Ciston, J.; Salahuddin, S. Enhanced ferroelectricity in ultrathin films grown directly on silicon. *Nature* **2020**, *580*, 478-482.

(56) Schlom, D. G.; Chen, L.-Q.; Eom, C.-B.; Rabe, K. M.; Streiffer, S. K.; Triscone, J.-M. Strain Tuning of Ferroelectric Thin Films. *Annual Review of Materials Research* **2007**, *37*, 589-626.

(57) Tybell, T.; Ahn, C. H.; Triscone, J.-M. Ferroelectricity in thin perovskite films. *Applied Physics Letters* **1999**, *75*, 856-858.

(58) Fong, D. D.; Stephenson, G. B.; Streiffer, S. K.; Eastman, J. A.; Auciello, O.; Fuoss, P. H.; Thompson, C. Ferroelectricty in Ultrathin Perovskite Thin Films. *Science* **2004**, *304*, 1650-1653.

(59) Choi, K. J.; Biegalski, M.; Li, Y. L.; Sharan, A.; Schubert, J.; Uecker, R.; Reiche, P.; Chen, Y. B.; Pan, X. Q.; Gopalan, V.; Chen, L.-Q.; Schlom, D. G.; Eom, C. B. Enhancement of Ferroelectricity in Strained BaTiO3 Thin Films. *Science* **2004**, *306*, 1005-1009.

(60) Trolier-McKinstry, S.: Crystal Chemistry of Piezoelectric Materials. In *Piezoelectric and Acoustic Materials for Transducer Applications*; Safari, A., Akdoğan, E. K., Eds.; Springer: Boston, M.A., 2008.

(61) Gradauskaite, E.; Campanini, M.; Biswas, B.; Schneider, C. W.; Fiebig, M.; Rossell, M. D.; Trassin, M. Robust In-Plane Ferroelectricity in Ultrathin Epitaxial Aurivillius Films. *Advanced Materials Interfaces* **2020**, 2000202.

(62) Garcia, V.; Fusil, S.; Bouzehouane, K.; Enouz-Vedrenne, S.; Mathur, N. D.; Barthélémy, A.; Bibes, M. Giant tunnel electroresistance for non-destructive readout of ferroelectric states. *Nature* **2009**, *460*, 81-84.

(63) Rodriguez, B. J.; Jesse, S.; Alexe, M.; Kalinin, S. V. Spatially Resolved Mapping of Polarization Switching Behavior in Nanoscale Ferroelectrics. *Advanced Materials* **2008**, *20*, 109-114.

(64) Luborsky, F. E.; Livingston, J. D.; Chin † , G. Y.: CHAPTER 29 - MAGNETIC PROPERTIES OF METALS AND ALLOYS. In *Physical Metallurgy (Fourth Edition)*; Cahn, R. W., Haasen † , P., Eds.; North-Holland: Oxford, 1996; pp 2501-2565.

(65) Zhang, D.; Sando, D.; Sharma, P.; Cheng, X.; Ji, F.; Govinden, V.; Weyland, M.; Nagarajan, V.; Seidel, J. Superior polarization retention through engineered domain wall pinning. *Nature Communications* **2020**, *11*, 349.

(66) Gruverman, A.; Alexe, M.; Meier, D. Piezoresponse force microscopy and nanoferroic phenomena. *Nature Communications* **2019**, *10*, 1661.

(67) Dahan, D.; Molotskii, M.; Rosenman, G.; Rosenwaks, Y. Ferroelectric domain inversion: The role of humidity. *Applied Physics Letters* **2006**, *89*, 152902.

(68) Li, J.-B.; Huang, Y. P.; Rao, G. H.; Liu, G. Y.; Luo, J.; Chen, J. R.; Liang, J. K. Ferroelectric transition of Aurivillius compounds Bi5Ti3FeO15 and Bi6Ti3Fe2O18. *Applied Physics Letters* **2010**, *96*, 222903.

(69) Funakubo, H. Degradation-free dielectric property using bismuth layer-structured dielectrics having natural superlattice structure. *Journal of the Ceramic Society of Japan* **2008**, *116*, 1249-1254.

(70) Maksymovych, P.; Huijben, M.; Pan, M.; Jesse, S.; Balke, N.; Chu, Y.-H.; Chang, H. J.; Borisevich, A. Y.; Baddorf, A. P.; Rijnders, G.; Blank, D. H. A.; Ramesh, R.; Kalinin, S. V. Ultrathin limit and dead-layer effects in local polarization switching of BiFeO${}_{3}$. *Physical Review B* **2012**, *85*, 014119.

(71) Balke, N.; Choudhury, S.; Jesse, S.; Huijben, M.; Chu, Y. H.; Baddorf, A. P.; Chen, L. Q.; Ramesh, R.; Kalinin, S. V. Deterministic control of ferroelastic switching in multiferroic materials. *Nature Nanotechnology* **2009**, *4*, 868-875.

(72) Jesse, S.; Baddorf, A. P.; Kalinin, S. V. Dynamic behaviour in piezoresponse force microscopy. *Nanotechnology* **2006**, *17*, 1615-1628.

(73) Imai, A.; Cheng, X.; Xin, H. L.; Eliseev, E. A.; Morozovska, A. N.; Kalinin, S. V.; Takahashi, R.; Lippmaa, M.; Matsumoto, Y.; Nagarajan, V. Epitaxial Bi5Ti3FeO15–CoFe2O4 Pillar–Matrix Multiferroic Nanostructures. *ACS Nano* **2013**, *7*, 11079-11086.

(74) Keeney, L.; Schmidt, M.; Amann, A.; Maity, T.; Deepak, N.; Faraz, A.; Petkov, N.; Roy, S.; Pemble, M. E.; Whatmore, R. W.: Novel Approaches for Genuine Single-Phase Room Temperature Magnetoelectric Multiferroics. In *Nanoscale Ferroelectrics and Multiferroics*; John Wiley & Sons, Ltd, 2016; pp 789-829.

(75) Halpin, J. C.; Schmidt, M.; Maity, T.; Pemble, M. E.; Keeney, L. Compositional tuning of the Aurivillius phase material Bi5Ti3-2xFe1+xNbxO15 ($0 \leq x \leq 0.4$) grown by chemical solution deposition and its influence on the structural, magnetic and optical properties of the material. *IEEE Transactions on Ultrasonics, Ferroelectrics, and Frequency Control* **2020**, *doi: 10.1109/TUFFC.2020.2997406*.

(76) Boyn, S.; Grollier, J.; Lecerf, G.; Xu, B.; Locatelli, N.; Fusil, S.; Girod, S.; Carrétéro, C.; Garcia, K.; Xavier, S.; Tomas, J.; Bellaiche, L.; Bibes, M.; Barthélémy, A.; Saïghi, S.; Garcia, V. Learning through ferroelectric domain dynamics in solid-state synapses. *Nature Communications* **2017**, *8*, 14736.

(77) Luo, Z.-D.; Apachitei, G.; Yang, M.-M.; Peters, J. J. P.; Sanchez, A. M.; Alexe, M. Bi-ferroic memristive properties of multiferroic tunnel junctions. *Applied Physics Letters* **2018**, *112*, 102905.

(78) Baudry, L.; Lukyanchuk, I.; Vinokur, V. M. Ferroelectric symmetry-protected multibit memory cell. *Scientific Reports* **2017**, *7*, 42196.

SYNOPSIS TOC. The persistence of stable ferroelectricity close to unit-cell thickness in B6TFMO, in both in-plane and out-of-plane directions, is significant and initiates possibilities for miniaturizing novel multiferroic-based devices.

